



# Angle-controllable RNA tiles for programmable array assembly and RNA sensing

Received: 20 September 2024

Accepted: 3 April 2025

Published online: 19 April 2025

Check for updates

Qi Yang <sup>1</sup>, Xu Chang <sup>1</sup>, Jung Yeon Lee <sup>1</sup>, Henry Wisniewski <sup>1</sup>, You Zhou <sup>2,3</sup>, Ashley D. Bernstein <sup>4</sup>, Edward M. Bonder <sup>5</sup>, Jason T. Kaelber <sup>4</sup>, Teresa Wu <sup>2,3</sup>, Giulia Pedrielli <sup>2,3</sup> & Fei Zhang <sup>1</sup>

Programmed self-assembly of RNA nanostructures presents a strategic approach to developing biomaterials with tailored properties and functionalities. Despite advancements, the variety, complexity, and programmability of de novo engineered RNA nanostructures remain limited. Here, we introduce a category of artificially designed RNA tiles by integrating antiparallel crossovers and T-junctions, featuring a controllable angle of either 65° or 90°. A total of 22 distinct tiles are explored, significantly expanding the collection of artificially designed multi-stranded RNA tiles. We investigate the design strategies that affect array assembly including T-loop configuration, sticky end pairing, structural diversification, and variations in annealing methods. Additionally, one single-stranded TC-RNA tile is designed and folded co-transcriptionally, suggesting promising applications in synthetic biology and molecular engineering. Furthermore, we demonstrate the integration of split broccoli RNA aptamers into the multi-stranded monomer tiles, enabling fluorescence activation along linear arrays for programmable RNA sensing. The facile incorporation with RNA functional nanostructures highlights the vast potential of these RNA tiles in constructing more sophisticated nanostructures for diverse biomaterial applications.

The self-assembly of biomolecules, such as proteins, DNA, and RNA, has become a practical approach to developing functional biomaterials for biotechnological and biomedical applications<sup>1,2</sup>. As a vital bio-polymer, RNA naturally exhibits a broad spectrum of chemical, structural, and functional diversities. Therefore, the development of deliberately engineered artificial RNA nanostructures has gained prominence in synthetic biology<sup>3</sup>, metabolic engineering<sup>4</sup>, and therapeutics<sup>5</sup>. These RNA nanostructures are primarily based on either rearranged natural RNA motifs or design strategies adapted from DNA tiles<sup>6,7</sup>. For example, RNA nanocages were constructed by modifying the packaging RNA of bacteriophage Phi29, taking advantage of its

natural T-shaped secondary structure<sup>8</sup>. RNA double crossover tiles and RNA homooligomeric nanostructures were inspired by the design of DNA double crossover tiles and branched kissing-loop motifs, respectively<sup>6,9</sup>.

Although DNA nanostructure design principles provide a valuable framework, the variety and complexity of artificially engineered RNA nanostructures currently available are comparatively limited<sup>10</sup>. The unique attributes and challenges associated with RNA require careful consideration when designing RNA tiles. The presence of an additional 2'-hydroxyl group in RNA significantly influences its stability and folding properties, resulting in different assembly

<sup>1</sup>Department of Chemistry, Rutgers University, Newark, NJ 07102, USA. <sup>2</sup>School of Computing and Augmented Intelligence, Arizona State University, Tempe, AZ 85281, USA. <sup>3</sup>ASU-Mayo Center for Innovative Imaging, Arizona State University, Tempe, AZ 85281, USA. <sup>4</sup>Rutgers CryoEM & Nanoimaging Facility, Rutgers University, Piscataway, NJ 08854, USA. <sup>5</sup>Department of Biological Sciences, Rutgers University, Newark, NJ 07102, USA. e-mail: [fei.zhang@rutgers.edu](mailto:fei.zhang@rutgers.edu)

behaviors and requirements<sup>11</sup>. RNA molecules are more prone to forming complex secondary structures, such as hairpins and bulges, compared to DNA. Additionally, artificial RNA tiles adopt A-form helices, while artificial DNA tiles typically feature B-form helices. The A-form helix is characterized by inclined hydrogen bonds, in contrast to the parallel hydrogen bonds found in the B-form helix<sup>12</sup>. These differences emphasize the importance of developing design strategies specifically tailored to the unique properties of RNA molecules to unlock their full potential for creating diverse and complex nanostructures.

Beyond structural design, RNA plays an important role in cellular processes<sup>13,14</sup>. It acts as a template for protein synthesis and can be secreted by disease-related cells<sup>15,16</sup>, making RNA detection essential for understanding cellular mechanisms and diagnosing diseases. RNA aptamers, known for their high specificity and binding affinity, have been developed for various applications including diagnostics, molecular detection, biomarker discovery, therapeutics, and drug delivery<sup>17-20</sup>. By integrating RNA aptamers into rationally designed RNA structures, we can create materials that are both sophisticated and multifunctional<sup>21</sup>.

Additionally, DNA nanostructures face delivery challenges due to their reliance on endocytosis via the endosome pathway *in vivo*<sup>22-24</sup>, leading to limited efficiency. Rapid degradation and clearance from the blood also further hinder their stability. Current solutions involve chemical modifications, such as PEGylation and endosome-escape peptides<sup>25,26</sup>. However, RNA nanostructures present a unique solution by leveraging co-transcriptional folding, allowing cellular transcription machinery to generate RNA materials directly inside cells. Recent studies highlight co-transcriptionally folded RNA as promising materials for biomedical applications *in vivo*<sup>9,27-29</sup>. In this work, we develop diverse RNA nanostructures, while showcasing co-transcriptional folding capability, and demonstrating RNA sensing *in vitro*, which will serve as a strong foundation for future *in vivo* applications.

In this research, we create 22 RNA tiles capable of assembling into either one-dimensional (1D) or 2D arrays with controllable angles (Fig. 1a, b). These tiles feature a T-junction loop (T-loop) and anti-parallel crossovers are named as TC-RNA tiles. The angle between the horizontal and vertical arm can be precisely adjusted by modifying the length of the T-loop. Specifically, T-loops of 6 nucleotides (nt) or 8 nt produce angles of 90° or 65°, respectively. We explore the crucial

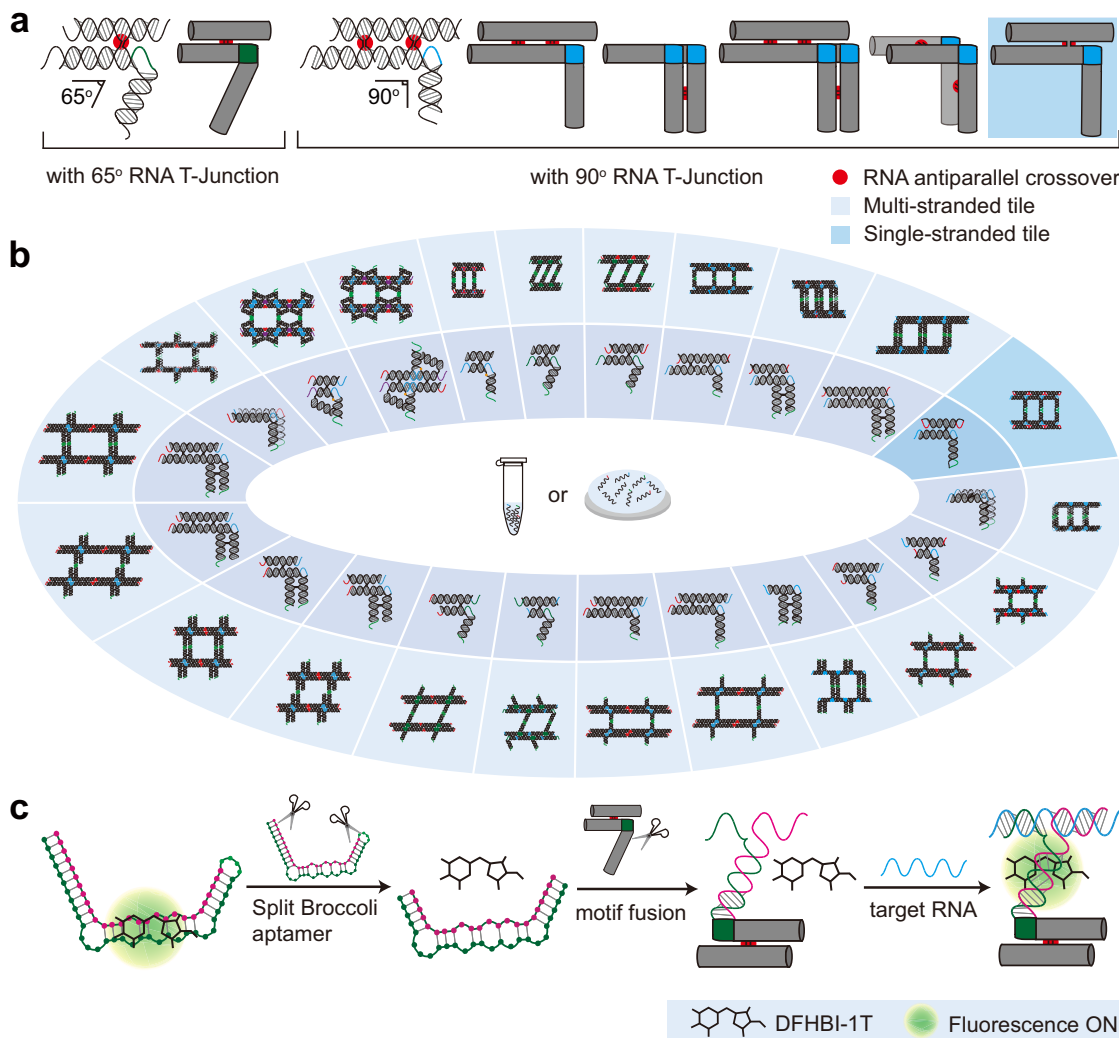


**Fig. 1 | A category of artificially designed TC-RNA tiles and their corresponding arrays.** **a** The design of RNA TC-RNA tiles contains an artificial 65° RNA T-junction (colored in green) or an artificial 90° RNA T-junction (colored in blue). The red circles highlight the locations of crossovers. The intrinsic angle of the artificial RNA T-junction is controlled by the nucleotide length of the T-loop region. For example, the 6 nt T-loop will form an off-plane 90° angle, while the 8 nt T-loop form an

in-plane 65° angle. Note that a single-stranded TC-RNA tile, designed for cotranscriptional folding, is highlighted with a blue background. **b** Schematics of 21 TC-RNA tiles and arrays. Two annealing methods, in solution and on mica, are employed. **c** Split RNA broccoli aptamers functionalized TC-RNA tiles for target RNA sensing. Fluorescence ON is triggered by the irradiation of UV light.

design parameters for de novo RNA tile design, including the matching rules and locations of sticky ends, the placement of unpaired nucleotides, strut structure, and arm stiffness. To demonstrate its potential for future *in vivo* applications, a co-transcriptionally folded single-stranded TC-RNA tile is designed and shown to form a ladder structure. Furthermore, we demonstrate the functionalization of TC-RNA tiles by introducing split broccoli aptamers into monomer tiles, enabling fluorescence turn-on upon target RNA presence (Fig. 1c).

## Results

### Design of angle-controllable TC-RNA tiles

Unlike double-stranded DNA with a B-form helix, RNA adopts an A-form (Supplementary Fig. 1). The inclination of the hydrogen bond makes the RNA T-junction geometrically different from DNA T-junctions<sup>30</sup>. Adapting from DNA T-junction design strategies, we introduced three types of RNA T-junctions: T1, T2 and T3 (Supplementary Fig. 2). The schematics show that a DNA T-junction, featuring an in-plane 6 nt T-loop, possess a 90° angle. In contrast, RNA T-junctions vary: T1, with a 6 nt T-loop at the center, forms an off-plane 90° angle; T2, incorporating an elongated 8 nt T-loop, maintains an in-plane orientation and natural connection, resulting in an in-plane 65° angle; T3 introduces an 8 nt T-loop and an unpaired nucleotide at the joint, enhancing the flexibility of the vertical arm and aiming for an in-plane 90° angle.

Drawing on DNA tile design strategies, we can control the rigidity and angled geometry of an RNA tile by integrating unpaired nucleotides and strut structures<sup>31</sup>. We first designed two tiles, TC-RNA-1 and TC-RNA-2, based on RNA T-junction T3 and T2, respectively. The atomic force microscopy (AFM) and native gel results confirmed our predictions, showing that these tiles formed angle-controlled ladder structures (Supplementary Figs. 3–5). This indicates that an unpaired nucleotide at the joint can change the angle of an RNA tile from 65° to 90°. Then we tested two tiles with struts, TC-RNA-3 and TC-RNA-4, to investigate whether the flexibility introduced by an unpaired nucleotide could be stabilized by strut structures (Supplementary Fig. 6). The AFM images showed twists and mismatches in both arrays, suggesting that struts cannot fully compensate for the flexibility generated by the unpaired nucleotide.

We hypothesize that the structural design of sticky ends, T-junction joints, and arm rigidity are critical factors in assembling TC-RNA tiles into large arrays. The guiding principles for our study on 1D and 2D assembly included: placing sticky ends at the 5' end to avoid the elongation or shortening at the 3' sticky ends during transcription, using unequal lengths of sticky ends within the same tile to reduce mismatches between different pairs, investigating RNA T-junctions (T1 and T2) that do not have an unpaired nucleotide at the joint for precise control over the angle of TC-RNA tiles, and incorporating crossovers into horizontal and/or vertical arms of the RNA tiles to ensure their stable formation. In addition, sequence design is crucial for the correct assembly of RNA tiles. Sequences for the TC-RNA tiles were generated by Tiamat and evaluated by NU-ResNet and NUPACK<sup>32–34</sup>. The criteria for sequence design included the following: each RNA strand must start with at least one G at the 5' end, avoid incorporating G-U wobble pairs, limit repeating bases to six nucleotides, minimize secondary structures in the DNA template from which the RNA strand is transcribed, and the G/C content in the RNA sequences is between 40% and 60%.

### Self-assembly of TC-RNA tiles into ladders

To demonstrate that the angle of TC-RNA tiles can be controlled by the length of T-loop, we designed tiles TC-RNA-5 and TC-RNA-6 (Fig. 2a) by employing RNA T-junctions T2 (with a 6 nt T-loop) and T1 (with an 8 nt T-loop), respectively. Both tiles aimed to assemble into ladder structures. After annealing in solution for 12 h, the native gel images showed an aggregation on top indicating the formation of target ladders

(Supplementary Figs. 7, 8). AFM further confirmed that both tiles formed the target ladder configurations (Fig. 2b and Supplementary Figs. 9, 10). As expected, TC-RNA-2 produced ladders with a right angle (-90°), whereas TC-RNA-1 formed ladders with an acute angle (-65°), as confirmed by transmission electron microscopy (TEM) imaging (Fig. 2a, b and Supplementary Fig. 11). These findings suggested that the angle of TC-RNA tiles can be modulated by adjusting the T-loop length.

Subsequently, we designed three TC-RNA tiles to evaluate the effect of reinforcing the arms with double helices by incorporating crossovers. Tile TC-RNA-7 and TC-RNA-8 were engineered with a vertical arm strengthened by one antiparallel crossover and one or two antiparallel crossovers strengthened horizontal arm. The AFM images showed that both tiles assembled into ladders with angles nearing 90° (Fig. 2a and Supplementary Figs. 12–14). The native gel data suggested the formation of large aggregates (Supplementary Fig. 14). We employed cryo-electron tomography (cryoET) to analyze the assemblies of TC-RNA-8, revealing a mix of configurations including linear, branched, and ring-shaped ladders (Fig. 2c). Measurements of the vertical and horizontal spacing of the ladders in one tomogram are summarized in Supplementary Fig. 15, showing that the observed dimensions of the RNA tile in this image closely match the designed model. Tile TC-RNA-9 contained off-plane, two-layered helices by overlapping two RNA T-junction helices and tightening them up through antiparallel crossovers on both horizontal and vertical arms. AFM imaging revealed a right-handed twist in the ladders, indicating an intrinsic twist of the double-layer monomer tile (Supplementary Fig. 16). From the study on these three tiles, we concluded that the reinforcement of the tile arms is preferable for the in-plane one-layer helices rather than the off-plane multi-layered ones.

We tested a single-stranded TC-RNA tile, TC-RNA-10, designed for co-transcriptional folding. Four conditions were explored: co-transcriptional folding in solution, co-transcriptional folding on mica, thermo-annealing in solution, and thermo-annealing on mica. AFM images confirmed that all four conditions successfully formed the target ladders (Fig. 2d and Supplementary Fig. 17). Among them, thermo-annealing in solution produced the longest and most well-formed ladders. In contrast, co-transcriptional folding on mica led to the formation of shorter half-ladder nanostructures, likely due to the surface-assisted method restricting the mobility of the initially formed half-ladders during assembly.

### Self-assembly of TC-RNA tiles into grids

To investigate the factors influencing the 2D array formation of TC-RNA tiles, we explored a variety of design and experimental parameters. These included the configuration of T-junctions, rules for matching sticky ends, the lengths of arms, the placement of crossovers, and annealing conditions. In total, we designed 12 tiles (TC-RNA-11 to TC-RNA-22) for 2D array self-assembly. Seven tiles had a double helix arm and a double helices arm, and five tiles had two double helices arms. Each tile was subjected to four different annealing conditions: in solution TAE, in solution HEPES, on mica in TAE, and on mica in TAB (see Methods for the detailed annealing conditions). The in-solution annealed samples were characterized by native gel, revealing large aggregates across all samples (Supplementary Figs. 7, 8, 14, 18–21). Comparing the AFM images of the samples under the four different annealing conditions, the on-mica annealing programs generally produce larger and more regular grids than those in-solution annealing methods.

As shown in Fig. 3a, tile TC-RNA-11 and TC-RNA-12 have the same structural design but different sticky-end matching rules (Fig. 3). For example, to enclose one rhomboid shape inside the 2D patterns, tile TC-RNA-11 required four monomer tiles while tile TC-RNA-12 required six. The AFM images showed that both tiles formed target acute-angled grids, and the on-mica TAB annealing method generated larger array

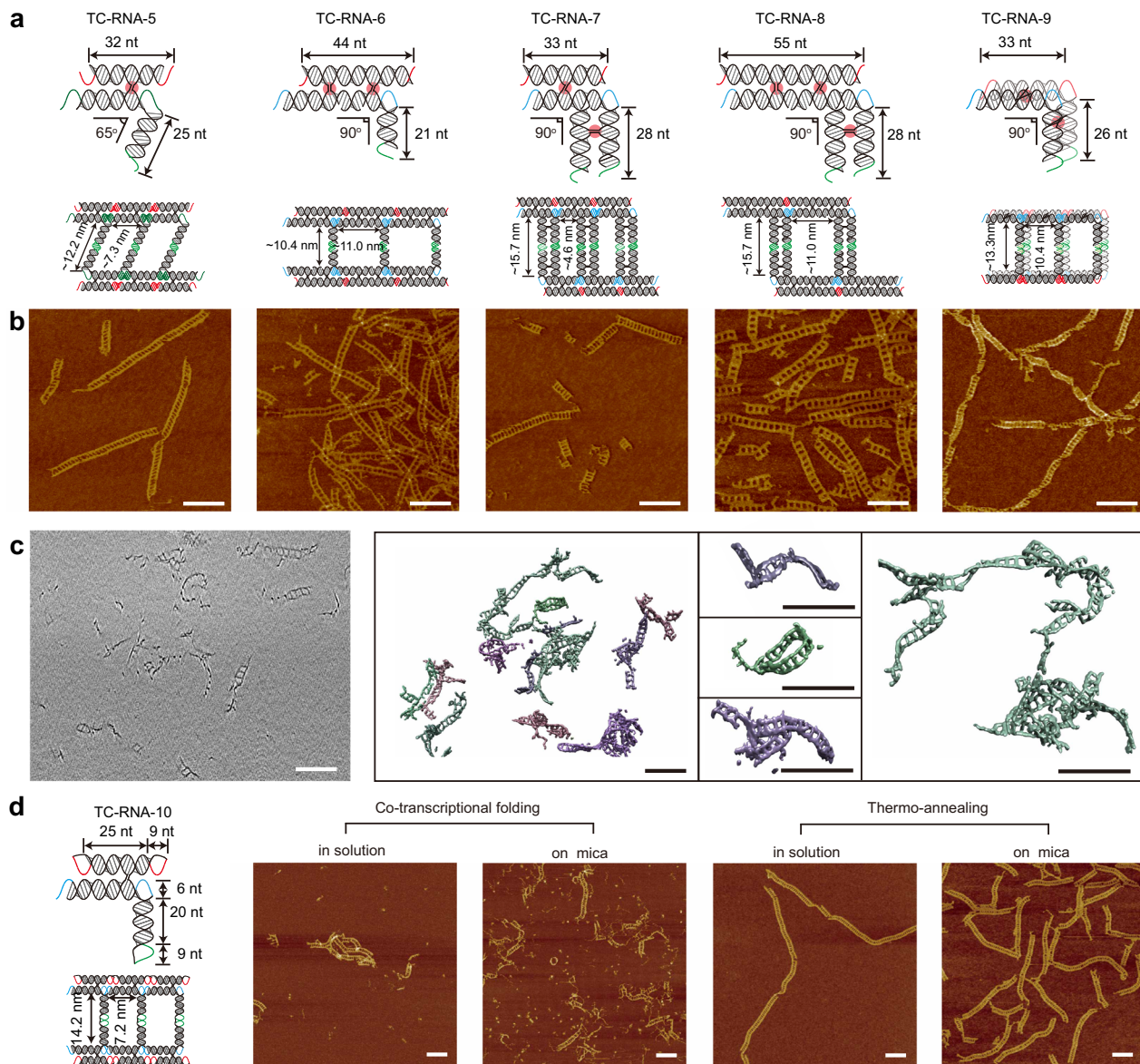


**Fig. 2 | Self-assembly of TC-RNA tiles to ladders.** **a** The design schematic showcases five TC-RNA tiles alongside their corresponding assembled ladders. Colored region indicates complementary sticky end pairing. Each complementary sticky-end-sticky-end pair or sticky-end-T-loop pair is labeled with the same color. The red circles highlight the locations of crossovers. The blue circles label the locations of crossovers. **b** AFM images of assembled arrays. From left to right, the arrays are assembled from tile TC-RNA-5, tile TC-RNA-6, tile TC-RNA-7, tile TC-RNA-8, and tile TC-RNA-9, respectively. All the AFM images are taken after annealing in 1×TAE  $Mg^{2+}$  buffer from 70 °C to 15 °C for 12 h. The scale bar is 100 nm for all images. **c** Cryo-EM

and tomography reconstruction images of TC-RNA-8. Left, slice through a tomogram of TC-RNA-8; right, 3D segmentation of that tomogram with individual particles visualized in insets. **d** The design schematic and AFM images of single-stranded TC-RNA-10 tile. The AFM images of cotranscriptional folding in solution and on mica are taken after annealing in 1×TAE  $Mg^{2+}$  buffer at 37 °C for 1 h. The AFM images of thermos-annealing in solution and on mica are taken after annealing in 1×TAE  $Mg^{2+}$  buffer from 70 °C to 15 °C for 12 h. All AFM images in this figure were reproduced at least three times, with each experiment conducted independently. The scale bar is 100 nm for all images.

pieces than the on-mica TAE (Supplementary Figs. 22, 23). Similar results were also found in tiles TC-RNA-13 and TC-RNA-14 (Fig. 3 and Supplementary Figs. 24, 25), indicating different sticky-end match rules could be adapted to form different 2D patterns. Notably, tile TC-RNA-11 self-assembled into tubular arrays when annealed in TAE solution, while tile TC-RNA-13 formed small flat array pieces under the same buffer conditions, suggesting that an 8 nt T-loop brings a more flexible center than that of a 6 nt T-loop (Supplementary Figs. 24, 26).

Further, we designed tile TC-RNA-15 and TC-RNA-16 with 21 nt and 28 nt lengths of vertical arms, respectively (Fig. 3a and Supplementary Figs. 27, 28). Both tiles share identical horizontal arms reinforced by two antiparallel crossovers. AFM results revealed that TC-RNA-15 formed more regular grids than TC-RNA-16 in 1×TAE  $Mg^{2+}$  buffer. This

difference in assembly was attributed to two factors. First, the longer arm of tile TC-RNA-16 had more flexibility in the vertical direction. Second, the assembly pathway for tile TC-RNA-15 included a self-correction mechanism for any potential curvatures along the vertical direction, involving a 180° flip of alternative tiles along the X-axis. In contrast, tile TC-RNA-16 with a 180° rotation along the Y-axis, without flipping, tended to accumulate curvature (Supplementary Fig. 29). Additionally, tile TC-RNA-15 and tile TC-RNA-14 formed comparably sized 2D arrays, suggesting that the crossover numbers in monomer tile were not restricted for 2D array assembly in our TC-RNA tile systems.

We next tested the reinforcement on the vertical arm rather than on the horizontal arm by designing tile TC-RNA-17 with double

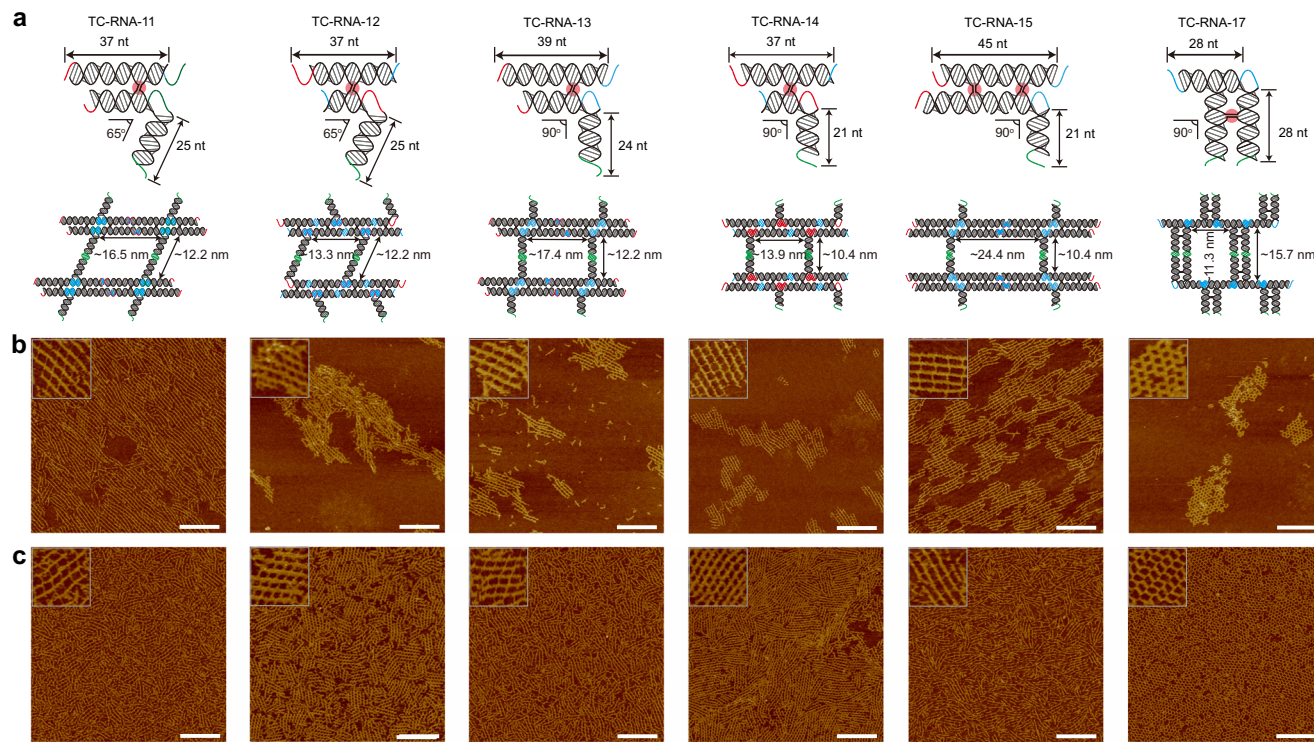


**Fig. 3 | 2D array self-assembly from TC-RNA tiles with a double helix arm.** **a** The design schematic showcases six TC-RNA tiles alongside their corresponding 2D array assemblies. The red circles indicate the locations of crossovers. **b** AFM images of assembled arrays of six TC-RNA tiles on mica assembly in 1xTAE  $Mg^{2+}$  buffer.

**c** AFM images of assembled arrays of six TC-RNA tiles on mica assembly in 1xTAB  $Mg^{2+}$  buffer. From left to right in panel (b) and (c), the arrays assembled from tile

TC-RNA-11, tile TC-RNA-12, tile TC-RNA-13, tile TC-RNA-14, tile TC-RNA-15, and tile TC-RNA-17, respectively. All the AFM images are taken after annealing from 70 °C to 15 °C for 12 h. All AFM images in this figure were reproduced at least three times, with each experiment conducted independently. The scale bar is 200 nm. The inset image size is 100 nm × 100 nm.

T-junctions including a double-helix horizontal arm and an antiparallel crossover between the two helices (Supplementary Fig. 30). Aligned with our design, AFM images of samples assembled on mica showed the formation of target grids (Fig. 3b, c), highlighting the effectiveness of the reinforced vertical arms in TC-RNA tiles design. Furthermore, tile TC-RNA-17 formed tubular structures under in-solution annealing in TAE buffers, indicating intrinsic curvature in the monomer tile (Supplementary Figs. 31, 32).

Subsequently, we created four TC-RNA tiles with reinforced vertical and horizontal arms and varying the number of crossovers and sticky ends (Fig. 4, TC-RNA-18 to TC-RNA-21). All four tiles formed smaller pieces under in-solution annealing (Supplementary Fig. 33). After on mica self-assembly, the two tiles with blunt ends formed smaller grid pieces, while the other two tiles with two sticky ends formed larger assemblies (Supplementary Figs. 34–37). It is suggested that sticky ends on the vertical arms of TC-RNA tiles are important for array self-assembly. Lastly, we demonstrated a two-layered tile TC-RNA-22 with stacked helices on both arms (Supplementary Fig. 38). Similar to the layer design for ladder assembly (Fig. 2, TC-RNA-17), the flexibility at the joint of the T-junction caused the formed small pieces of the array to twist and overlap with each other, resulting in tangled aggregates in 3D (Supplementary Fig. 39).

#### Incorporation of fluorescent aptamers on TC-RNA arrays

RNA aptamers exhibit sensitive and specific binding to target molecules such as proteins and small molecules<sup>35</sup>. Researchers have developed various RNA aptamer-functionalized nanostructures for applications in targeted drug delivery, molecular sensing, and therapeutic applications<sup>36,37</sup>. Multi-stranded TC-RNA tiles, as highly modular nanostructures, are particularly well-suited for incorporating aptamers, thus enabling customizable biosensing applications.

We explored this capability by integrating a split broccoli aptamer into TC-RNA tiles (Supplementary Fig. 40)<sup>38</sup>. As shown in Fig. 5a, two TC-RNA tiles containing RNA T-junction T2 and T1 were assembled into Array 1 and Array 2, respectively, displaying broccoli aptamer sequences on 65° or 90° vertical arms. Confirmation via AFM imaging showed that both arrays formed the target comb-like linear objects (Fig. 5b, c) and the native gel results showed the size difference between individual broccoli aptamers and the corresponding arrays (Supplementary Fig. 41). The activities of the aptamer-modified arrays were evaluated through fluorescence images and intensity measurements (Fig. 5d and Supplementary Fig. 42). Upon UV light irradiation, both Array 1 and Array 2, along with their respective individual aptamer controls, exhibited visible green fluorescence to the naked eyes, while no fluorescence was observed in the pure (5Z)-5-[(3,5-difluoro-4-hydroxyphenyl)methylene]-3,5-dihydro-2-methyl-3-(2,2,2-trifluoroethyl)-4H-imidazol-4-one (DFHBI-1T) dye control (Supplementary Figs. 42b, c). Quantitative analysis of normalized fluorescence intensity revealed that compared to the DFHBI-1T control, the fluorescence intensity of Broccoli control 1 and Array 1 increased by 99.6-fold and 138-fold, respectively and Broccoli control 2 and Array 2 increased by 147-fold and 129-fold, respectively. This data suggests that both arrays retained the fluorescence from the broccoli aptamers.

Next, we applied an AB half-ladder concept into the functionalized TC-RNA assemblies (Fig. 5e). The RNA broccoli aptamer was split into Strand 1 and Strand 2, integrated into two separated TC-RNA tiles. Annealing them separately would form two non-fluorescent arrays, Array 3 and Array 4. After mixing Array 3 and Array 4 at a 1:1 ratio (Array 3 + 4), Strand 1 and Strand 2 interacted to form the complete broccoli aptamer structure, activating fluorescence. The corresponding fluorescence intensity changes were recorded (Fig. 5f), where Arrays 3 and 4 were mixed at time 0, but no significant fluorescence change was

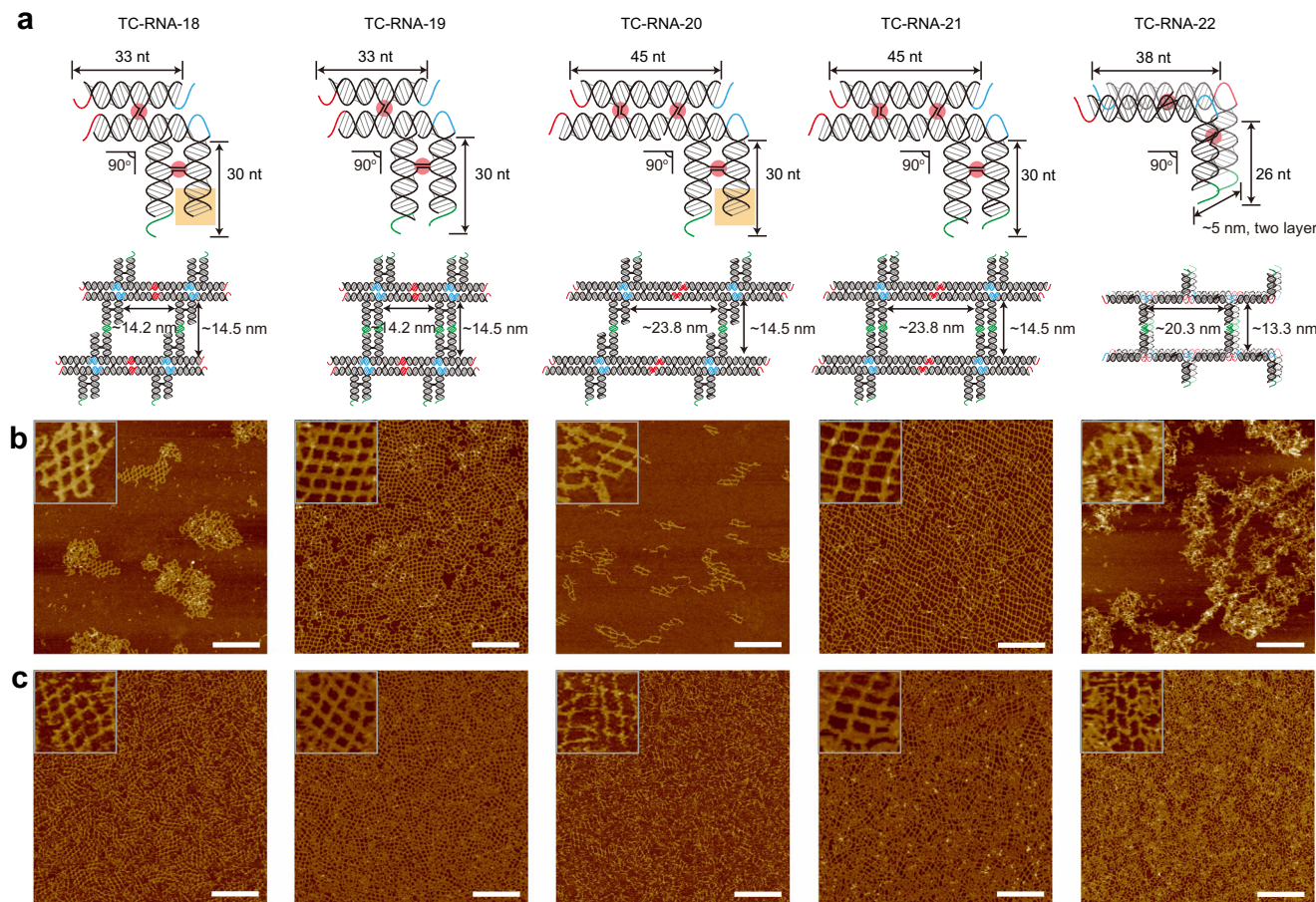


**Fig. 4 | 2D array self-assemble from TC-RNA tiles that with two double helices arms.** **a** The design schematic showcases the five TC-RNA tiles alongside their corresponding 2D array. The orange squares label the blunt end. The red circles indicate the locations of crossovers. **b** AFM images of assembled arrays of five TC-RNA tiles on mica assembly in 1xTAE  $Mg^{2+}$  buffer. **c** AFM images of assembled arrays of five TC-RNA tiles on mica assembly in 1xTAB  $Mg^{2+}$  buffer.

assembled arrays of five TC-RNA tiles on mica assembly in 1xTAB  $Mg^{2+}$  buffer. The order of AFM images matches the order of RNA tiles shown in panel (a). All the AFM images are taken after annealing from 70 °C to 15 °C for 12 h. All AFM images in this figure were reproduced at least three times, with each experiment conducted independently. The scale bar is 200 nm. The inset image size is 100 nm  $\times$  100 nm.

observed until the DFHBI-1T dye was added at approximately 5 min. The AFM images of Array 3 and Array 4 both showed a mixture of linear comb and ladders (Fig. 5g, h) due to the self-binding of Strand 1 in Array 3 and Strand 2 in Array 4. Array 3 + 4 mainly formed ladders under AFM (Fig. 5i and Supplementary Fig. 43) and showed a 68.9-fold increase in fluorescence intensity compared to the DFHBI-1T control (Fig. 5j), suggesting that functional broccoli aptamer structures were assembled between the two half ladders. Notably, the Broccoli control sample (Strand 1 + 2) had a 110-fold fluorescent increase, which was higher than Array 3 + 4. This difference possibly resulted from a small portion of uncompleted binding between the half ladders, which contained long single-stranded regions with strong secondary structures and mismatches. Overall, the AB half-ladder binding event triggered the fluorescence turn-on mechanism, allowing visualization of the specific interaction between Array 3 and 4. This approach enabled precise control over fluorescence activation by selectively assembling AB components, offering potential applications in monitoring binding events involving other targets such as enzymes and cells.

#### Split-aptamer-modified TC-RNA arrays for programmable RNA sensing

To further explore the potential of our system, we engineered two RNA sensing systems based on TC-RNA tiles by incorporating split broccoli aptamers (Fig. 6 and Supplementary Figs. 44–50). As illustrated in Fig. 6a, each monomer tile within Array 5 had two open ends of a split aptamer and a target RNA sensing domain named Strand A and Strand

B. In state 1, no fluorescence signal was detected as the broccoli structure remained unformed in the absence of the target RNA. Upon introducing the target RNA in state 2, the RNA sensing domain of the split aptamers binds the target RNA and stabilizes the broccoli structure, triggering an increase in fluorescence signal. In state 3, a DNA invader strand is introduced to displace the target RNA from Array 5 and shut off the signal. The programmable sequences of Strand A and B allow for easy adaptation to different RNA targets by adjusting their sequences. We assessed the sensing capability of our RNA arrays using two RNA derivatives from human KRAS mRNA and *E. coli* mreB mRNA<sup>39</sup>.

Experimentally, we engineered TC-RNA Array 5 to sense the KRAS derivative (Fig. 6a). AFM images showed clear differences between states: in state 1, only short linear arrays formed, whereas states 2 and 3 displayed longer linear arrays (Fig. 6b–d, Supplementary Fig. 44). Native gel images for state 1 had a smeared band without top aggregates, while state 2 and 3 both showed distinct top aggregates bands (Supplementary Fig. 45). The smaller assemblies in state 1 may result from insufficient stabilization by the 8 nt stem in Strand A and Strand B, compromising robust T-loop assembly at the joint (Supplementary Fig. 46a). In state 2, the target RNA binding enhanced T-loop stability, promoting larger array formation.

Quantitative fluorescence analysis revealed that directly transitioning state 1 to state 3 resulted in a 4.7-fold increase in fluorescence relative to the negative control, indicating that when target RNA and DNA invader are added simultaneously to state 1, the target RNA prefers binding with the DNA invader more than with strand A and B (Fig. 6e and

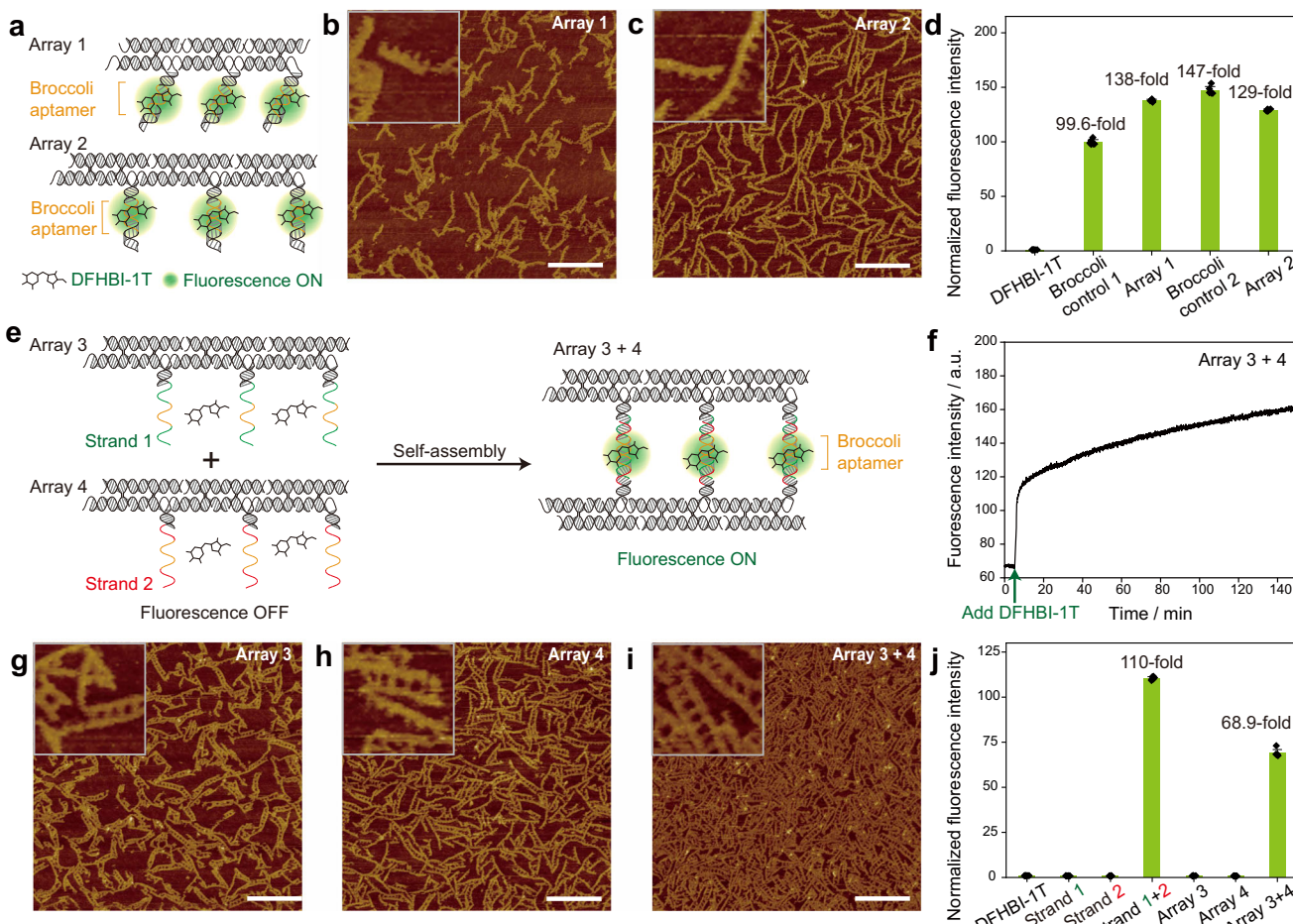


**Fig. 5 | Self-assembly of TC-RNA tiles with built-in RNA broccoli aptamer.** **a** Schematics of two linear assemblies by TC-RNA tiles with built-in RNA broccoli aptamer. **b**, **c** AFM images of Array 1 and Array 2. The scale bar is 200 nm. The inset image size is 100 nm  $\times$  100 nm. **d** The normalized fluorescence intensities of broccoli aptamer control, Array 1 and Array 2. **e** Schematics of fluorescence on AB arrays self-assembly. Individual tile array assembly (Array 3 or Array 4) cannot yield a fluorescence signal. The fluorescence turns on only after mixing Array 3 and Array 4 together, and the mix is named Array 3 + 4. **f** Kinetic tracing of the change in fluorescence intensity for the process described in panel (e). Arrays 3 and 4 are

mixed at 0 min, and the DFHBI-1T dye is added at approximately 5 min. The excitation wavelength is 470 nm, and the emission wavelength is 505 nm. **g–i** AFM images of Array 3, Array 4, and Array 3 + 4. The scale bar is 200 nm. **j** The normalized fluorescence intensity of control, Array 3, Array 4, and Array 3 + 4. For each assembled array, the same amount of RNA strands (0.5  $\mu$ M) was incubated in 40 mM HEPES (pH 7.4), 100 mM KCl, 1 mM MgCl<sub>2</sub>, and 10  $\mu$ M DFHBI-1T. AFM images were captured after a 2-h annealing process from 90 °C to 25 °C. Fluorescence intensities are presented as means  $\pm$  SEs from  $n = 6$  experiments (Ex = 470 nm and Em = 505 nm).

Supplementary Fig. 46). A 71.3-fold increase was observed when transitioning from state 1 to state 2, which was comparable to the 89-fold increase observed for the direct formation of state 2. However, transitioning from state 2 to state 3 resulted in a small decrease in fluorescence, suggesting that a 1:1 DNA invader to RNA target ratio was insufficient for effectively removing the target RNA. To address this, kinetic analysis was performed by adding different ratios of DNA invader to the state 2 of Array 5. As shown in Fig. 6f, fluorescence intensity decreased with prolonged incubation times and increased DNA invader ratios, indicating that a higher DNA invader ratio and longer incubation times enhance the removal efficiency of the target RNA. Additionally, an RNA dose-response curve for Array 5 was recorded (Supplementary Fig. 47a). State 1 of Array 5 (500 nM) was premixed with DFHBI-1T dye at a 1:20 ratio. The fluorescence intensity of Array 5 increased linearly as the target RNA concentration ranged from 1 nM to 500 nM (Fig. 6f). The lowest detectable concentration of target RNA was recognized as 10 nM, corresponding to approximately a 2.5-fold increase compared to the negative control. The dye response curve of Array 5 showed that the equilibrium was reached within 10 min (Fig. 6g), while the RNA target response curve stabilized around 1 h (Fig. 6h).

To assess the detection specificity of the RNA target, we compared the original RNA target sequence with seven RNA mutants (Fig. 6i and Supplementary Fig. 47b). The original RNA target, labeled as M0, served as a positive control, while M1–M7 represented the seven mutants. The results showed that fluorescence intensity decreased as the number of mutations increased, with Array 5 effectively detecting up to two nucleotide mutations. Specifically, M1 and M2, each containing a single nucleotide mutation, exhibited a 10–20% decrease in fluorescence intensity compared to the positive control. M3, which contained two nucleotide mutations, showed a dramatic drop, retaining only 6% of the fluorescence signal. Similarly, M6 and M7, with 9 and 13 nucleotide mutations, displayed fluorescence levels below 5% of the positive control. Beyond the number of mutations, their location also played a critical role. Interestingly, both M4 and M5 contained three mutations, but their effects differed significantly: while M5 retained 75% fluorescence intensity, M4 dropped to 3%. This discrepancy may be due to mutation positioning—M5's mutations were at the left edge of the target recognition region, leaving the central domain unaffected, allowing partial target RNA binding. Additionally, we designed TC-RNA arrays to detect a different RNA target, a mreB

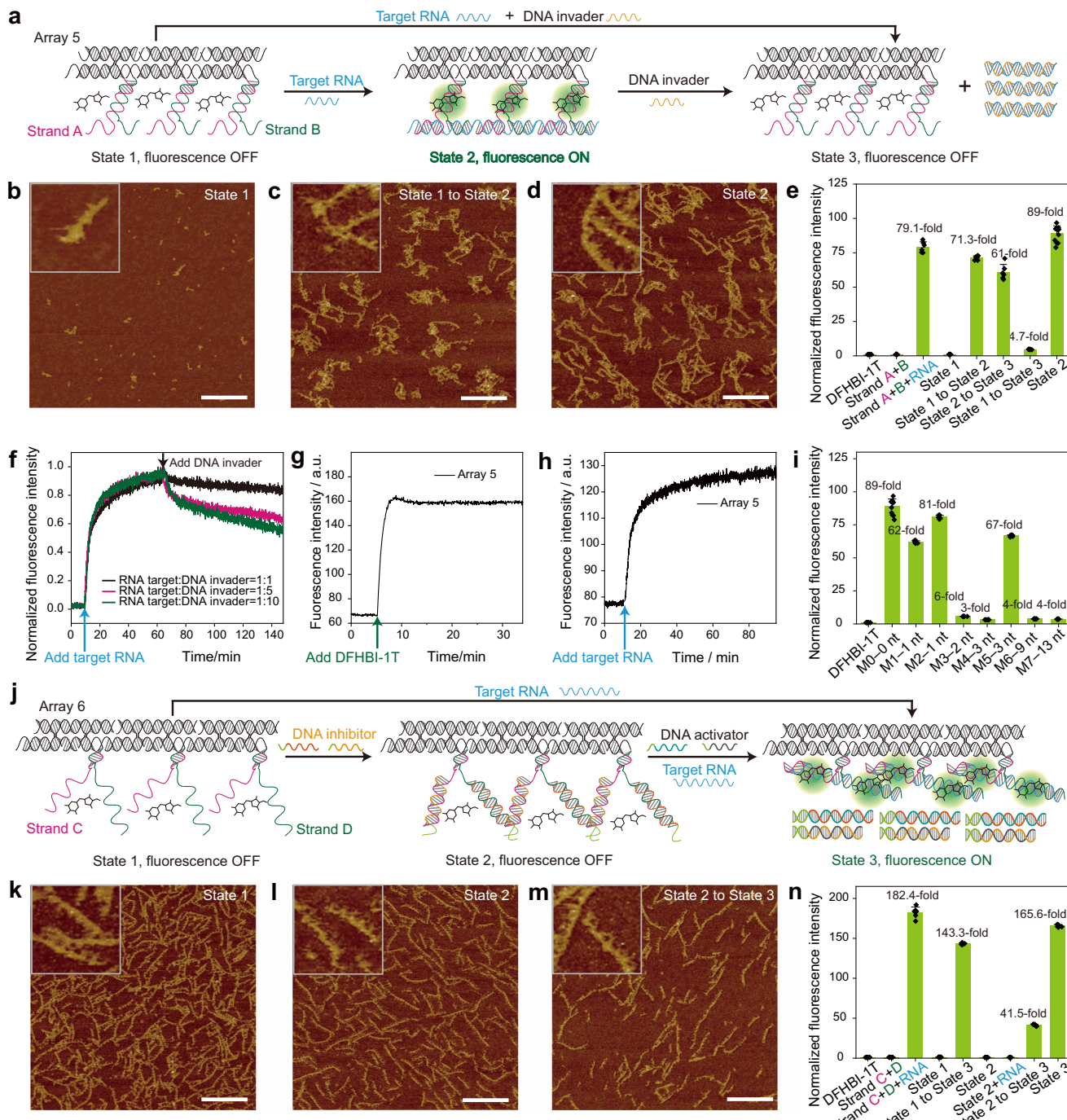


**Fig. 6 | Split-broccoli aptamer modified TC-RNA arrays for RNA sensing.**

**a** Schematics of a single broccoli aptamer functionalized TC-RNA tiles-based array for RNA sensing. Array 5 is initially fluorescence OFF at state 1 because of the flexible configuration of the split-broccoli aptamer. After target RNA stabilizes the split-broccoli aptamer at state 2, the fluorescence turns ON. At state 3, DNA invaders displace the target RNA, and the split-broccoli aptamer switches OFF again.

**b-d** AFM images of State 1 (direct annealed control), State 1 to State 2, and State 2 (direct annealed control). The scale bar is 200 nm. The inset image size is 100 nm x 100 nm. The scale bar is 200 nm. **e** The normalized fluorescence intensity of controls, State 1, State 1 to State 2, State 2 to State 3, State 1 to State 3, and State 2. **f** The kinetic comparison of the changes in fluorescence intensity in response to variations in the ratio between RNA target and DNA invader for Array 5. **g** The DFHBI-1T dye response curve of array 5. **h** The RNA target response curve of array 5. **i** The fluorescence intensity of Array 5 binding with different RNA targets. M0 is the original RNA target. M1 to M7 are mutant RNA targets.

**j** Schematics of two broccoli aptamer functionalized TC-RNA tiles-based arrays for RNA detection. The fluorescence will turn on when the presence of target RNA is detected. **k-m** AFM images of State 1 (direct annealed control), State 2 (direct annealed control), and State 2 to State 3. The scale bar is 200 nm. **n** The normalized fluorescence intensities of controls, State 1, State 1 to State 3, State 2, State 2+RNA, State 2 to State 3, and State 3 (direct annealed control). Note, for each assembled array, the same amount of RNA strands (0.5  $\mu$ M) was incubated with 40 mM HEPES (pH 7.4), 100 mM KCl, 1 mM MgCl<sub>2</sub>, and 10  $\mu$ M DFHBI-1T. AFM images were taken after a 2-h annealing program from 90 °C to 25 °C. The fluorescence intensities are calculated by the means  $\pm$  SEs of  $n = 6$  experiments (Ex = 470 nm and Em = 505 nm). The Array 5 state 2 in (e) is the same as the M0-0 nt in (i). The fluorescence intensities were calculated by the means  $\pm$  SEs of  $n = 12$  experiments, which were the combination of two batches of 6 independent measurements.

derivative, further demonstrating the feasibility of programmable RNA sensing (Supplementary Figs. 48, 49).

Finally, we designed another TC-RNA sensing structure, Array 6, by integrating two split broccoli aptamers into each monomer tile (Fig. 6j and Supplementary Fig. 50). In this design, we also introduced a turn-on mechanism via a DNA inhibitor strand, whereas the sensor will remain inactive until a DNA activator sequence is present. In the kinetic study of state 1 to state 3 transition in Array 6, no significant fluorescence changes were observed before or after adding the DNA activator to state 1. Fluorescence only occurred upon the introduction of the target RNA into the system (Supplementary Fig. 51a). Similar to Array 5, the dye response curve of Array 6 reached equilibrium within 10 min (Supplementary Fig. 51b), while the RNA target response curve reached equilibrium around 2 h (Supplementary Fig. 51c). Gel electrophoresis indicated a large array formation in all states (Supplementary Fig. 45, 48). AFM images revealed that by-product ladders in state 1, likely due to the mismatching caused by the single-stranded regions in Strand C and D (Fig. 6k). In contrast, state 2 and 3 displayed linear arrays because of the binding and stabilizing of Strand C and D by DNA inhibitor or target RNA (Fig. 6l, m & Supplementary Figs. 50, 52). Most notably, state 3 showed a significant increase in fluorescence, while state 1 and 2 did not fluoresce. The transition from state 2 to state 3 resulted in a 41.5-fold increase in fluorescence and direct annealing to state 3 led to a 165.6-fold increase (Fig. 6n). This fluorescence difference arises from the strand displacement reaction, where the DNA inhibitor and RNA target compete for binding to the aptamer domain. Moreover, by only adding target RNA to state 2 would result fluorescence OFF (State 2 + RNA), which indicated the RNA target and DNA activator were necessary factors for fluorescence turn on when transition from state 2 to state 3. We also evaluated the sensing process without the inhibitor and turn-on sequences. Direct transitioning from state 1 to state 3 resulted in a fluorescence increase of approximately 143.4-fold, which was comparable to the direct annealing of the structures in state 3. Compared to arrays with a single aptamer per tile (Array 5), the double-aptamer sensing array exhibited higher fluorescence intensity under identical conditions. This suggested that incorporating multiple aptamers into one tile can enhance fluorescence intensity without compromising array assembly.

## Discussion

The development of RNA nanotechnology has produced a variety of functional nanostructures for molecular recognition and biomedical applications through innovative RNA structural designs<sup>40,41</sup>. This study advanced 21 TC-RNA tiles for 1D and 2D assemblies and demonstrated the RNA sensing applications by integrating split aptamers into the arrays. It expanded the family of artificial RNA tiles and elucidated key design parameters for TC-RNA tiles. For the structural design, we identified three key factors: a T-junction with an appropriate loop length and no unpaired nucleotides, stick ends that ensured specific bindings, and a rigid arm reinforced by crossovers. Regarding sequence design, it was crucial to minimize unwanted secondary structures within individual strands and enhance the specificity of inter-strand pairing for target assembly. Additionally, a single-stranded TC-RNA tile was shown to fold and assemble into ladders under both isothermal co-transcriptional folding conditions and gradient thermo-annealing processes. Experimental conditions, such as buffer composition, surface assistance, and annealing program significantly influence the assembly of the RNA arrays.

The feasibility of easily functionalizing our TC-RNA assemblies was demonstrated through programmable RNA sensing. Future efforts could focus on incorporating different types of fluorescent aptamers to develop multiplex sensors or implementing molecular computing circuits into the array for intelligent sensing with logic gates. Additionally, the multi-stranded nature and distinctive geometry of the TC-RNA tiles allow for modification with functional RNA sequences such as

protein-binding RNA, ion-binding RNA, siRNA, microRNA, and anti-sense oligos<sup>42,43</sup>. Moving forward, TC-RNA tiles equipped with multiple functional groups could accelerate the development of next-generation molecular robots and serve as scaffolding elements or drug delivery vectors<sup>43</sup>. Since we have demonstrated the co-transcriptional folding of single-stranded TC-RNA in vitro, the multi-stranded tiles presented in this paper could also be adapted into single-stranded designs, further expanding the structural diversity of synthetic RNA nanostructures. Additionally, in vivo transcription provides a powerful approach to enhance the delivery efficiency and biocompatibility of functional RNA in living systems. Future research could explore the development of co-transcriptionally folded TC-RNA nanostructures optimized for in vivo applications. Overall, the TC-RNA tiles hold great potential for advancements in biomaterials, sensing, and therapeutics.

## Methods

### RNA sequence design and preparation

The structural and sequence design of TC-RNA tiles was first created in Tiamat and further evaluated by NU-ResNet and NUPACK<sup>32-34</sup>. The evaluation of the sequence and structure pairs using the NU-ResNet platform provided an idea of the likelihood of successful folding<sup>34</sup>. The detailed RNA sequences are listed in Supplementary Notes. The detailed sequences of primers and DNA templates used in this study are provided in the Source Data file. Each designed RNA strand was transcribed from a corresponding DNA template with T7 polymerase guided transcription in vitro (AmpliScribe T7-Flash transcription kit, #ASF3507, Epicenter, Inc.). DNA templates were purchased from Integrated DNA Technologies (IDT). DNA templates and in vitro transcribed RNA strands were purified by denaturing polyacrylamide gel electrophoresis (PAGE), followed by ethanol precipitated, and suspended in ultrapure water. Nanodrop 2000 (Thermo Scientific) was used to determine concentrations of nucleic acids.

### Polyacrylamide gel electrophoresis (PAGE)

**Denaturing PAGE:** The components of denaturing PAGE gel were ammonium persulfate (APS), urea, ultrapure water, acrylamide/bis-acrylamide 19:1, 40% solution, and Tetramethylethylenediamine (TEMED). The denaturing PAGE gels were cast at room temperature for 3 h before electrophoresis and run at 37 °C and 45 A in 1× TBE buffer. After electrophoresis, the gels were stained for 5 min with SYBR® Safe Nucleic Acid Gel Stain (Invitrogen, #S33102) for the DNA template or SYBR® Green Nucleic Acid Gel Stain (Invitrogen, # S7585) for RNA transcripts, respectively. Then, the gels were imaged using a Bio-rad gel imaging system.

**Non-denaturing PAGE:** The gel was prepared with pre-mix Acrylamide/bis-acrylamide 19:1, 40% solution, 10 × TAE Mg<sup>2+</sup> buffer, APS, and TEMED with appropriate concentrations, then cast at room temperature for 3 h before use. Gels were run at 4 °C at 200 V in 1× TAE Mg<sup>2+</sup> buffer. After electrophoresis, the gels were stained with gel red (Millipore sigma, SCTI23) and imaged by a Bio-rad gel imaging system.

### TC-RNA tiles self-assembly

**In solution self-assembly:** Each RNA strand was individually transcribed, gel extracted and purified, then suspended in ultrapure water. The OD of each RNA strand was measured after gel purification. Each RNA strand was mixed at a 1:1 ratio in an annealing buffer with a final concentration of 0.5 μM and then annealed in a thermocycler. Annealed samples were directly electrophoresed or imaged by AFM. Note, in-solution self-assembly used two annealing buffers, 1× TAE-Mg<sup>2+</sup> buffer and HEPES buffer, with annealing programs of 70 to 15 °C in 12 h and 90 to 25 °C in 2 h, respectively.

**On mica self-assembly:** A freshly cleaved mica was placed in a small petri dish, and then 80 μL of annealing buffer was added to the mica surface. A 0.5 μM sample mix was prepared, and 5 μL of the

sample mix was added to the mica surface. The petri dish was covered and annealed in a thermocycler from 70 to 15 °C over 12 h. Annealed samples were directly electrophoresed or imaged by AFM.

**Cotranscriptional folding:** DNA templates were commercially synthesized and purified by Integrated DNA Technologies. The cotranscriptional folding mix included 1X transcription buffer, 200 nM DNA templates, 1 mM dithiothreitol (DTT), and 25 mM rNTPs, and was initiated by the addition of T7 RNA polymerase (5% v/v). For cotranscriptional folding in solution, the reaction mix (20  $\mu$ L) was directly annealed in a PCR tube using a thermocycler at 37 °C for 2 h. For cotranscriptional folding on mica, the reaction mix was diluted 10-fold with 1X transcription buffer and added to freshly cleaved mica placed in a small petri dish (80  $\mu$ L). The petri dish was covered and annealed in a thermocycler at 37 °C for 2 h. Note: The 1X transcription buffer is prepared by diluting the 10X transcription buffer with ultrapure water. All transcription reagents are from the AmpliScribe T7-Flash Transcription Kit (Catalog #ASF3507, Epicenter, Inc.).

### Annealing conditions

Annealing buffers: 1×TAE-Mg<sup>2+</sup> buffer: 20  $\mu$ M Tris-acetate buffer, 2 mM EDTA, 12.5 mM MgCl<sub>2</sub>, and at pH 7.6; 1×TAB-Mg<sup>2+</sup> buffer: 20  $\mu$ M Tris-acetate buffer, 45 mM boric acid, 4 mM MgCl<sub>2</sub>, 45 mM NaCl, 45 mM KCl, and at pH 7.6; HEPES buffer: 40 mM HEPES, 100 mM KCl, 1 mM MgCl<sub>2</sub>, and at pH 7.4.

**Annealing program:** For the assembly of ladders and 2D arrays, 2 h, and 12 h annealing programs were used. The split-broccoli aptamer functionalized linear array assembly used the 2 h program.

**2 h program:** 90 °C to 2 min; 85 °C to 70 °C at 5 °C per minute; 69 °C to 38 °C at 1 °C per minute, 37 °C for 30 min; 30 °C for 30 min; then held at 25 °C.

**12 h program:** 70 °C to 54 °C at 1 °C per 5 min; 53 °C to 41 °C at 1 °C per 10 min; 40 °C to 21 °C at 1 °C per 25 min; then held at 15 °C.

The four annealing conditions were abbreviated as in solution TAE, in solution HEPES, on mica TAE, and on mica TAB.

### Fluorescence measurement

The fluorescence of DFHBI-1T dye control, split-broccoli aptamer control, and split-broccoli aptamer functionalized TC-RNA linear arrays were measured in a buffer (40 mM HEPES pH 7.4, 100 mM KCl, 1 mM MgCl<sub>2</sub>, pH 7.4, 10  $\mu$ M DFHBI-1T) at a total volume of 50  $\mu$ L. The DFHBI-1T (cat. no. SML2697-5MG) was purchased from Sigma-Aldrich. The concentration of Broccoli aptamer control and split-broccoli aptamer functionalized TC-RNA linear arrays was 0.5  $\mu$ M for fluorescence measurement. The DNA invader, DNA inhibitor, DNA activator, and RNA targets mentioned in this work are added 1 to a 1 ratio compared to each RNA strand (0.5  $\mu$ M). All the samples were incubated with DFHBI-1T dye at 37 °C for 30 min before fluorescence measurement. The fluorescence spectrums were measured using an excitation wavelength of 470 nm and an emission range from 485 to 700 nm. All the quantitative fluorescence intensity analyses were obtained by using a HORIBA Fluorolog-3 spectrophotometer. The fluorescence intensity data of emission at 505 nm were used for quantitative analysis. The formula for converting the raw fluorescence data to normalized values is: Normalized Fluorescence = (Fluorescence of Sample)/(Average Fluorescence of DFHBI-1T dye). All the kinetic analysis data were collected by using a Cary Eclipse spectrophotometer. The means  $\pm$  SEs were calculated based on six individual experiments ( $n = 6$ ).

### AFM imaging

**In solution annealed sample:** 5  $\mu$ L of annealed sample (0.5  $\mu$ M) pre-mixed with 1×TAE Mg<sup>2+</sup> buffer (70  $\mu$ L) was added onto a freshly prepared mica (Ted Pella), then NiCl<sub>2</sub> (100 mM, 2  $\mu$ L) solution was added and incubating for 5 min. The remained solution was blotted away by Kimwipes. Then 1×TAE Mg<sup>2+</sup> Buffer (70  $\mu$ L) and NiCl<sub>2</sub> solution

(100 mM, 2  $\mu$ L) were added, and the sample underwent AFM imaging. Images were collected by using ScanAsyst-fluid+ probe (Bruker) on a Bruker Fastcan AFM in the 'ScanAsyst in liquid' mode.

**On mica annealed sample:** The mica from the petri dish was taken out and left on a flat bench. 1×TAE Mg<sup>2+</sup> buffer (70  $\mu$ L) was added and left for 5 min. The top solution was gently removed by lightly touching a corner of filter paper to the edge of the mica. Then 1×TAE Mg<sup>2+</sup> Buffer (70  $\mu$ L) and NiCl<sub>2</sub> solution (100 mM, 2  $\mu$ L) were added and incubating for 5 min. The top solution of the mica was removed with filter paper. Then 1×TAE Mg<sup>2+</sup> Buffer (70  $\mu$ L) and NiCl<sub>2</sub> solution (100 mM, 2  $\mu$ L) were added before AFM imaging. Images were collected by using a ScanAsyst-fluid+ probe (Bruker) on a Bruker Fastcan AFM in the 'ScanAsyst in liquid' mode.

### TEM imaging

Transmission electron microscopy (TEM) images were collected using a Thermo Fisher FEI Tecnai 12 electron microscope, which was operated at 80 kV and equipped with a GATAN OneView 4K-by-4K CMOS camera. A 3  $\mu$ L of annealed RNA solution (5  $\mu$ L, 500 nM) was deposited onto a glow-discharged carbon-coated copper grid (Electron Microscopy Sciences) and incubated for 3 min. The excess solution was gently blotted away by filter paper. The sample was then negatively stained with 5  $\mu$ L of 0.75% (w/v) uranyl formate for 1 min. After air drying overnight, the samples were processed for TEM analysis without further treatment.

### Cryo-electron tomography

3  $\mu$ L of TC-RNA-8 at 5  $\mu$ M in 1×TAE-Mg<sup>2+</sup> buffer was preincubated on a 200 mesh R2/2 Quantifoil grid with a 2 nm continuous carbon coating (Electron Microscopy Sciences) for 7 min. Then, vitrification was conducted using a Vitrobot Mark IV (Thermo Fisher Scientific) with 3 seconds of blotting and 95% chamber humidity. Tilt series of TC-RNA-8 were collected on a Talos Arctica cryo-electron microscope (Thermo Fisher Scientific) equipped with a K2 camera (Gatan) using the SerialEM acquisition software. Tilt series were acquired at 2.134  $\text{\AA}/\text{pixel}$  with a 100  $\mu$ M objective aperture inserted and target defocus ranging from -3.5  $\mu$ m to -8  $\mu$ m. The accumulated dose per tilt series was 90 electrons/ $\text{\AA}^2$ . The tilt series was acquired in a dose-symmetric fashion with 35 steps at 4° per step in groups of 4 tilt steps or 47 steps in 3° increments in groups of 5. The representative tomogram shown in Fig. 2c was acquired from -60° to +60° in 4° step increments in groups of 4 with a target defocus of -8  $\mu$ m, and continuous carbon was not visible in the tilt series, indicating a lack of coverage of continuous carbon in that region.

Motion correction was performed in SerialEM at the time of acquisition. Tomogram generation was performed in the IMOD software package with patch-tracking (no fiducials), CTF correction by phase-flipping of tilted micrographs, and SIRT for reconstruction. Tomograms were filtered with nonlinear anisotropic diffusion and segmented using Segger during visualization with UCSF Chimera.

### Statistics and reproducibility

The data statistics in the manuscript are based on six independent experiments. Each experimental condition was reproduced at least three times or more for AFM image collection, optimization of annealing and imaging protocols, and control experiments.

### Reporting summary

Further information on research design is available in the Nature Portfolio Reporting Summary linked to this article.

### Data availability

The data supporting the findings of this study are available within the main text and its Supplementary Information. The raw data and statistical analysis of fluorescence intensity in this study are provided in

the Source Data files. Source data is available for Fig. 3b, c, Fig. 4b, c, Fig. 5b-d, f-j, Fig. 6b-i&k-n, and Supplementary Figs. 42b-d, 43b-d, 46b-d, 47a, 49b-e, and 50b-d in the associated Source Data files. Source data are provided with this paper.

## References

1. Li, S. et al. A DNA nanorobot functions as a cancer therapeutic in response to a molecular trigger in vivo. *Nat. Biotechnol.* **36**, 258–264 (2018).
2. Yang, Q. et al. Recent advances in self-assembled DNA nanostructures for bioimaging. *ACS Appl. Bio Mater.* **5**, 4652–4667 (2022).
3. Vezza, G. E., Gadila, L. R. & Salis, H. M. Automated design of protein-binding riboswitches for sensing human biomarkers in a cell-free expression system. *Nat. Commun.* **14**, 2416 (2023).
4. Na, D. et al. Metabolic engineering of *Escherichia coli* using synthetic small regulatory RNAs. *Nat. Biotechnol.* **31**, 170–174 (2013).
5. Paunovska, K., Loughrey, D. & Dahlman, J. E. Drug delivery systems for RNA therapeutics. *Nat. Rev. Genet.* **23**, 265–280 (2022).
6. Stewart, J. M., Subramanian, H. K. K. & Franco, E. Self-assembly of multi-stranded RNA motifs into lattices and tubular structures. *Nucleic Acids Res.* **45**, 5449–5457 (2017).
7. Guo, S. et al. Ultra-thermostable RNA nanoparticles for solubilizing and high-yield loading of paclitaxel for breast cancer therapy. *Nat. Commun.* **11**, 972 (2020).
8. Hao, C. et al. Construction of RNA nanocages by re-engineering the packaging RNA of Phi29 bacteriophage. *Nat. Commun.* **5**, 3890 (2014).
9. Liu, D. et al. Branched kissing loops for the construction of diverse RNA homooligomeric nanostructures. *Nat. Chem.* **12**, 249–259 (2020).
10. Krissanaprasit, A. et al. Self-assembling nucleic acid nanostructures functionalized with aptamers. *Chem. Rev.* **121**, 13797–13868 (2021).
11. Velema, W. A. & Kool, E. T. The chemistry and applications of RNA 2'-OH acylation. *Nat. Rev. Chem.* **4**, 22–37 (2020).
12. Heinemann, U. & Roske, Y. Symmetry in nucleic-acid double helices. *Symmetry* **12**, 737 (2020).
13. Liu, S. et al. A tRNA-derived RNA fragment plays an important role in the mechanism of arsenite-induced cellular responses. *Sci. Rep.* **8**, 16838 (2018).
14. Wang, J. et al. RNA structure profiling at single-cell resolution reveals new determinants of cell identity. *Nat. Methods* **21**, 411–422 (2024).
15. Marchingo, J. M. & Cantrell, D. A. Protein synthesis, degradation, and energy metabolism in T cell immunity. *Cell Mol. Immunol.* **19**, 303–315 (2022).
16. Toyama, Y. & Shimada, I. NMR characterization of RNA binding property of the DEAD-box RNA helicase DDX3X and its implications for helicase activity. *Nat. Commun.* **15**, 3303 (2024).
17. Szliszka, E. et al. Ethanolic extract of propolis (EEP) enhances the apoptosis-inducing potential of TRAIL in cancer cells. *Molecules* **14**, 738–754 (2009).
18. Zhang, Y., Lai, B. S. & Juhas, M. Recent advances in aptamer discovery and applications. *Molecules* **24**, 941 (2019).
19. Kruger, A. et al. Aptamer applications in emerging viral diseases. *Pharmaceuticals (Basel)* **14**, 622 (2021).
20. Wang, Y. et al. Recent advance of RNA aptamers and DNAzymes for MicroRNA detection. *Biosens. Bioelectron.* **212**, 114423 (2022).
21. Chang, X. et al. Reconfigurable DNA nanocage for protein encapsulation and regulation. *J. Am. Chem. Soc.* **146**, 26131–26138 (2024).
22. Pinheiro, A. V. et al. Challenges and opportunities for structural DNA nanotechnology. *Nat. Nanotechnol.* **6**, 763–772 (2011).
23. Afonin, K. A. et al. Opportunities, barriers, and a strategy for overcoming translational challenges to therapeutic nucleic acid nanotechnology. *ACS Nano* **14**, 9221–9227 (2020).
24. Tian, T., Li, Y. & Lin, Y. Prospects and challenges of dynamic DNA nanostructures in biomedical applications. *Bone Res.* **10**, 40 (2022).
25. Keller, A. & Linko, V. Challenges and perspectives of DNA nanostructures in biomedicine. *Angew. Chem. Int. Ed. Engl.* **59**, 15818–15833 (2020).
26. Smolkova, B. et al. Protein corona inhibits endosomal escape of functionalized DNA nanostructures in living cells. *ACS Appl. Mater. Interfaces* **13**, 46375–46390 (2021).
27. Li, M. et al. In vivo production of RNA nanostructures via programmed folding of single-stranded RNAs. *Nat. Commun.* **9**, 2196 (2018).
28. Pothoulakis, G., Nguyen, M. T. A. & Andersen, E. S. Utilizing RNA origami scaffolds in *Saccharomyces cerevisiae* for dCas9-mediated transcriptional control. *Nucleic Acids Res.* **50**, 7176–7187 (2022).
29. Zhang, T. et al. Programmable in vitro and in vivo folding of single-stranded nucleic-acid wireframe origami. *Chem* **10**, 2550–2563 (2024).
30. Yang, Q. et al. DNA T-shaped crossover tiles for 2D tessellation and nanoring reconfiguration. *Nat. Commun.* **14**, 7675 (2023).
31. Liu, L. et al. Rational design and self-assembly of two-dimensional, dodecagonal DNA quasicrystals. *J. Am. Chem. Soc.* **141**, 4248–4251 (2019).
32. Williams, S. et al. *Tiamat: A Three-Dimensional Editing Tool for Complex DNA Structures* 90–101 (Springer Berlin Heidelberg, 2009).
33. Zadeh, J. N. et al. NUPACK: Analysis and design of nucleic acid systems. *J. Comput. Chem.* **32**, 170–173 (2011).
34. Zhou, Y. et al. Predicting RNA sequence-structure likelihood via structure-aware deep learning. *BMC Bioinformatics* **25**, 316 (2024).
35. Lu, X., Kong, K. Y. S. & Unrau, P. J. Harmonizing the growing fluorogenic RNA aptamer toolbox for RNA detection and imaging. *Chem. Soc. Rev.* **52**, 4071–4098 (2023).
36. Kara, N. et al. Aptamers targeting membrane proteins for sensor and diagnostic applications. *Molecules* **28**, 3728 (2023).
37. Zhou, H., Li, Y. & Wu, W. Aptamers: promising reagents in biomedicine application. *Adv. Biol. (Weinh.)* **8**, e2300584 (2024).
38. Alam, K. K. et al. A fluorescent split aptamer for visualizing RNA-RNA assembly in vivo. *ACS Synth. Biol.* **6**, 1710–1721 (2017).
39. Furuhata, Y. et al. Programmable RNA detection with a fluorescent RNA aptamer using optimized three-way junction formation. *RNA* **25**, 590–599 (2019).
40. Jasinski, D. et al. Advancement of the emerging field of RNA nanotechnology. *ACS Nano* **11**, 1142–1164 (2017).
41. Chandler, M. et al. The International Society of RNA Nanotechnology and Nanomedicine (ISRNN): the present and future of the burgeoning field. *ACS Nano* **15**, 16957–16973 (2021).
42. Crooke, S. T. et al. Antisense technology: an overview and prospectus. *Nat. Rev. Drug Discov.* **20**, 427–453 (2021).
43. Sargazi, S. et al. siRNA-based nanotherapeutics as emerging modalities for immune-mediated diseases: a preliminary review. *Cell Biol. Int.* **46**, 1320–1344 (2022).

## Acknowledgements

This work is supported by a US National Science Foundation grant 2007821 and a faculty Startup Fund from Rutgers University to F.Z., grant 2007861 to G.P. and T.W., and grant DK119198 to E.M.B. We acknowledge the Cryo-EM facilities at the Rutgers Cryo-EM & Nanoimaging Facility and the electron microscopy facilities of the Department of Biological Sciences, Laboratory for Advanced Imaging.

## Author contributions

Q.Y. and F.Z. conceived the idea. Q.Y. and X.C. designed the structures. Q.Y., X.C., Y.Z., T.W., and G.P. designed and evaluated the sequences for

multi-stranded TC-RNA tile. X.C. and Q.Y. assigned the sequences and characterized the single-stranded TC-RNA tile. Q.Y., X.C., and J.L. prepared and characterized samples. Q.Y., X.C., J.L., H.W., and F.Z. performed the data analysis. A.D.B. and J.T.K. froze and imaged the samples for CryoET and processed corresponding data. E.M.B. provided TEM technical support. The manuscript was written through the contributions of all authors. All authors have given approval to the final version of the manuscript.

## Competing interests

The authors declare no competing interests.

## Additional information

**Supplementary information** The online version contains supplementary material available at  
<https://doi.org/10.1038/s41467-025-58938-5>.

**Correspondence** and requests for materials should be addressed to Fei Zhang.

**Peer review information** *Nature Communications* thanks the anonymous, reviewers for their contribution to the peer review of this work. A peer review file is available.

**Reprints and permissions information** is available at  
<http://www.nature.com/reprints>

**Publisher's note** Springer Nature remains neutral with regard to jurisdictional claims in published maps and institutional affiliations.

**Open Access** This article is licensed under a Creative Commons Attribution-NonCommercial-NoDerivatives 4.0 International License, which permits any non-commercial use, sharing, distribution and reproduction in any medium or format, as long as you give appropriate credit to the original author(s) and the source, provide a link to the Creative Commons licence, and indicate if you modified the licensed material. You do not have permission under this licence to share adapted material derived from this article or parts of it. The images or other third party material in this article are included in the article's Creative Commons licence, unless indicated otherwise in a credit line to the material. If material is not included in the article's Creative Commons licence and your intended use is not permitted by statutory regulation or exceeds the permitted use, you will need to obtain permission directly from the copyright holder. To view a copy of this licence, visit <http://creativecommons.org/licenses/by-nc-nd/4.0/>.

© The Author(s) 2025